RSC Advances

ROYAL SOCIETY OF CHEMISTRY

PAPER

View Article Online
View Journal | View Issue

Check for updates

Cite this: *RSC Adv.*, 2026, **16**, 21667

Enhanced photocatalytic degradation of Congo red by a $BiVO_4/ZnIn_2S_4$ composite: performance and mechanism

Xinyue Liu,[a,b] Yixin Zhang,[b] Jiaxing Yu[b] and Ming Li *[b]

High-performance visible-light-driven photocatalysts have emerged as a research hotspot in environmental pollution; however, the photocatalytic degradation mechanisms of Congo red using bismuth semiconductor composites are not fully understood. Herein, $BiVO_4/ZnIn_2S_4$ was successfully synthesized *via* a hydrothermal method, and the photocatalytic performance of the composite was assessed by carrying out photocatalysis experiments to decompose Congo red. The phase composition, carrier separation capability, interface electron interactions, and morphological features were characterized by XRD, PL, XPS, and TEM analyses, respectively. The results showed that a Z-scheme heterostructure was successfully constructed between the $BiVO_4$ and $ZnIn_2S_4$. Electrons in the conduction band of $BiVO_4$ migrated to the valence band of $ZnIn_2S_4$, which effectively enhanced the separation of photogenerated charge carriers and improved the degradation capability. Compared with pure $BiVO_4$, 7% $BiVO_4/ZnIn_2S_4$ displayed superior photocatalytic capability and could completely remove Congo red (100 mg L^{-1}) in 60 min under visible light. Radical trapping experiments combined with electron paramagnetic resonance characterization revealed that the superoxide anion ($^{\bullet}O_2^-$) and holes (h^+) acted as the key reactive species driving Congo red degradation. In addition, six cycles of experiments were performed to verify that the $BiVO_4/ZnIn_2S_4$ composite retains its high stability. This study provides a feasible strategy for fabricating effective photocatalysts to treat organic pollutants in wastewater.

Received 28th January 2026
Accepted 26th March 2026

DOI: 10.1039/d6ra00765a

rsc.li/rsc-advances

1 Introduction

Water is essential for life on Earth and the basic guarantee of human reproduction and life. Unfortunately, due to the rapid development of printing and dyeing industries, the discharge of dyestuff wastewater has dramatically increased.[1] Wastewater containing synthetic organic dyes can harmfully affect the structure of aquatic communities.[2] As a typical benzidine direct azo dye, Congo red is widely used in the textile, paper-making, rubber, and plastics industries; however, it can induce allergic reactions and is metabolically converted into benzidine. Due to the high stability of Congo red,[3] removing it from industrial wastewater is extremely difficult. To ensure the safety of drinking water, wastewater containing toxic substances should be treated before being released into the environment. Various biological and physicochemical methods, *e.g.*, membrane filtration,[4] precipitates,[5] ion exchange,[6] biodegradation,[7] and adsorption[8] have been employed to treat wastewater. However, these conventional approaches are inefficient and have limitations; *e.g.*, membrane filtration and precipitate techniques are expensive and produce hazardous secondary contaminants and waste materials.[9] Although anaerobic digestion is cost-effective, it struggles to fully mineralize the recalcitrant organic compounds such as Congo red due to slow microbial metabolic rates and poor tolerance to toxic pollutants, and it is also highly susceptible to fluctuations in environmental conditions.[10] Advanced oxidation processes (such as the Fenton process[11] and photocatalysis) have been demonstrated to be the most effective to fully eliminate organic pollutants from wastewater. The Fenton process has been widely applied in this field due to its strong oxidizing capacity.[12] Furthermore, in recent years, photocatalytic technology has been widely used to remove pollutants, produce hydrogen and ammonia, and regulate the nitrogen cycle[13] due to its excellent oxidation capacity, environmental friendliness, compatibility, long-term high efficiency, and economic sustainability.[14] The photocatalytic process is independent of microbial activity and can rapidly mineralize organic pollutants under visible light, showing a broader degradation spectrum, faster reaction rates, and stronger resistance to interference. Therefore, the development of novel photocatalysts can provide an effective technique to deal with wastewater pollution. Among the visible-light photocatalytic materials, bismuth-based photocatalysts are

---

[a] *Nanjing-Helsinki Institute in Atmospheric and Earth System Sciences, Nanjing University, Suzhou 215163, China*

[b] *College of Forestry, Northeast Forestry University, Harbin 150040, China. E-mail: liming1986@nefu.edu.cn; Tel: +86-451-82192120*

considered outstanding visible-light-driven photocatalytic materials due to their narrow band gap (E_g) of less than 3.0 eV.[15] Notably, bismuth vanadate ($BiVO_4$) has attracted great research attention because of the unique optical, electrical properties, and promising photocatalytic performance. $BiVO_4$ effectively absorbs visible light, significantly improving its solar energy utilization efficiency and overcoming the low efficiency limitations of UV photocatalysts such as TiO_2. However, its catalytic performance is constrained by a narrow specific surface area and suboptimal separation of photogenerated electron–hole pairs. To achieve the separation of photogenerated carriers, the construction of heterojunctions has become a novel research hotspot. $BiVO_4$ possesses sufficient valence-band potential to generate holes and reactive oxygen species with robust oxidative capacity.[16] Accordingly, a range of $BiVO_4$-based catalysts have been developed for diverse applications; *e.g.*, $Fe_3N/BiVO_4$ was used for H_2 generation,[17] $BiVO_4/g\text{-}C_3N_4/rGO$ and $BiVO_4/TiS_2$ were employed to enhance pollution degradation,[18] $CdS/BiVO_4$ was adopted for CO_2 reduction,[19] and $MoS_2/BiVO_4$ was applied for bacterial disinfection.[20]

Zinc indium sulfide ($ZnIn_2S_4$) is a metal–thiolate material with a layered spinel structure that has drawn considerable interest due to its prominent photoelectric response and environmental stability.[21] The interlayer bonding *via* van der Waals forces provides a rapid transport channel for photogenerated carriers, effectively suppressing bulk recombination. Z-scheme $Bi_2S_3/ZnIn_2S_4$ heterostructures have been successfully synthesized to enhance charge separation and transport rate, boosting photogenerated carrier separation and improving methylene blue photodegradation efficiency.[22] Notably, the $BiVO_4/ZnIn_2S_4$ Z-scheme heterojunction photocatalytic system can be further activated by introducing $NaBH_4$ and peroxymonosulfate. Analysis of the band structure and charge transfer mechanism indicates that the composite system has excellent potential for photocatalytic coupling with advanced oxidation processes [23,24]. The E_g of $ZnIn_2S_4$ is 2.6 eV, and the conduction band (CB) value is below zero, which means that it can absorb more visible light.[25] Given that $BiVO_4$ and $ZnIn_2S_4$ have similar E_g values, and the CB value of $ZnIn_2S_4$ is much lower than that of $BiVO_4$, these two materials possess a matched band structure and complementary light absorption ranges that are ideal for constructing suitable heterojunctions to further improve the photocatalytic performance of $BiVO_4$.

Herein, a direct Z-scheme heterostructure $BiVO_4/ZnIn_2S_4$ photocatalyst was fabricated. Subsequently, photocatalytic degradation of Congo red by the $BiVO_4/ZnIn_2S_4$ photocatalyst was investigated. A possible photocatalytic mechanism describing the $BiVO_4/ZnIn_2S_4$ system was also proposed.

2 Experiment

2.1 Synthesis of catalysts

$Bi(NO_3)_3 \cdot 5H_2O$ (4.85 g, 0.001 mol) was dissolved in 20 mL of HNO_3 solution, which was recorded as solution A. Furthermore, NH_4VO_3 (1.17 g, 0.001 mol) and EDTA (1.99 g, 0.0068 mol) were dissolved in NaOH solution (40 mol L^{-1}, 20 mL) and labeled as solution B. Subsequently, solution B was gradually added to solution A, the mixture was stirred for 30 minutes, and its pH was adjusted to 5. Then the mixture (70 mL) was slowly injected into a 100 mL Teflon-lined stainless-steel autoclave and hydrothermally treated at 180 °C for 24 hours. After heating, the sediments were collected *via* filtration, rinsed with water and ethanol to eliminate impurities, and finally dried at 65 °C to yield pure $BiVO_4$.[26]

$ZnCl_2$ (0.136 g, 1 mmol), $InCl_3 \cdot 4H_2O$ (0.586 g, 2 mmol), and CH_3CSNH_2 (TAA) (0.3 g, 4 mmol) were fully dissolved in deionized water. A defined amount of the pre-synthesized $BiVO_4$ solid was dispersed into the above-mentioned mixture to attain $BiVO_4/ZnIn_2S_4$ samples with weight ratios of 7%, 15%, and 25%. After sonicating for 1 hour, the mixture (40 mL) was slowly injected into a Teflon-lined stainless-steel autoclave and hydrothermally treated at 180 °C for 12 hours. When the hydrothermal reaction was complete, the resulting precipitates were collected by filtration, rinsed with deionized water and ethanol to eliminate impurities, and finally dried at 65 °C to obtain a $BiVO_4/ZnIn_2S_4$ [27,28].

2.2 Photocatalytic experiments

Catalysts (50 mg) with different ratios were dispensed into separate solutions of Congo red (100 mL and 400 mg L^{-1}). Before light irradiation, the suspensions were stirred in the dark for 30 minutes to establish adsorption–desorption equilibrium between the catalyst and Congo red. Subsequently, degradation experiments were conducted using a cylindrical photochemical reactor fitted with a simulated sunlight source. The Congo red solution was decomposed under irradiation from a 300 W xenon lamp (equipped with a 420 nm cutoff filter). Every 10 minutes, 2 mL of liquid was taken and filtered through a 0.22 μm membrane. The concentration of Congo red was measured using a UV-Vis spectrophotometer (Shimadzu UV3600, Japan).

To further clarify the major reactive species dominating the photocatalytic reaction, three scavengers were introduced: benzoquinone (BQ, 0.1 mmol L^{-1}), triethanolamine (TEOA, 10 mmol L^{-1}), and isopropanol (IPA, 10 mmol L^{-1}) to target superoxide radicals ($^{\bullet}O_2^-$), holes (h^+), and hydroxyl radicals ($^{\bullet}OH$), respectively.

2.3 Characterization

The crystalline phase of the samples was studied by X-ray diffraction (XRD, TD-3500, China) . To study the surface morphology and microstructure, scanning electron microscopy (SEM, Gemini 300, ZEISS, Germany), high-resolution transmission electron microscopy (TEM, JEOL JEM-2100F, Japan), and energy-dispersive spectrometry (EDS) analyses were utilized. Additionally, X-ray photoelectron spectroscopy (XPS, Thermo Fisher, USA) was adopted to verify the samples' elemental compositions and surface. A Brunauer–Emmett–Teller (BET, Quantachrome, Autosorb iQ) instrument was used to determine the pore properties and specific surface areas. Functional group information was characterized *via* Fourier-transform infrared spectroscopy (FT-IR, Nicolet Nexus 670, USA) analysis. Photoluminescence (PL) spectra were recorded with a Hitachi fluorescence spectrophotometer (FLS980, UK).

Trapping experiments and electron paramagnetic resonance (EPR, Shimadzu, Japan) measurements were conducted to identify the active species participating in the photocatalytic reaction. Finally, the UV-vis diffuse reflectance spectra (DRS) of the synthesized photocatalysts were collected with a UV-vis spectrophotometer (Shimadzu UV3600, Japan).

3 Results and discussion

3.1 Characterization of catalysts

Fig. 1 presents the XRD spectra of $BiVO_4/ZnIn_2S_4$ composite samples with different $BiVO_4$ mass fractions. The patterns of the composite materials exhibit the characteristic diffraction peaks corresponding to the monoclinic phase $BiVO_4$ (ref. 29) (PDF# 14-0688) and the hexagonal crystal type $ZnIn_2S_4$ (ref. 30) (PDF# 72-0773). The distinct peaks observed at 2θ values of 28.82°, 30.54°, 39.78°, 46.71°, and 47.30° matched with the (−121), (040), (211), (240), and (042) planes of $BiVO_4$, respectively; meanwhile, the distinct peaks at 21.58°, 27.69°, 47.17°, 52.21°, 52.44°, and 75.47° corresponded to the (006), (102), (110), (112), (116), and (211) crystal planes of $ZnIn_2S_4$, respectively, confirming that the composite contained $BiVO_4/ZnIn_2S_4$.

As shown in Fig. 2a, decahedral $BiVO_4$ presents a smooth monoclinic phase. As shown in Fig. 2b, $ZnIn_2S_4$ presents a folded layer, which would contribute to an expanded specific surface area and an increased number of active sites, enhancing the separation efficiency between electrons and holes. As can be seen in Fig. 2c, $BiVO_4$ is anchored to the $ZnIn_2S_4$ surface, forming tight contacts without changing the morphology of the $ZnIn_2S_4$. However, the $BiVO_4/ZnIn_2S_4$ composite has a coarser surface than pure $ZnIn_2S_4$, which expands the reaction area and enhances its photocatalytic activity. As shown in Fig. 2g, the sample exhibits distinct rod-like structures with uniform distribution. These structures have been confirmed as $BiVO_4$ and are well-dispersed on the surface of the $ZnIn_2S_4$ matrix. The rods exhibit a typical length of several hundred nanometers and a diameter of tens of nanometers. This unique rod-like morphology not only increases the specific surface area of the composite, providing more active sites for the adsorption and degradation of Congo red, but also shortens the migration distance of photogenerated carriers, facilitating their separation and transfer at the heterojunction interface. The corresponding EDS elemental mapping (Fig. 2h) further confirmed that the Bi, V, O, Zn, S, and In elements were evenly distributed in the synthesized materials and highly dispersed in the selected area, indicating that strong interactions between $BiVO_4$ and $ZnIn_2S_4$ were formed. This can accelerate the charge separation rate and mitigate the charge recombination rate during photocatalytic degradation.[31]

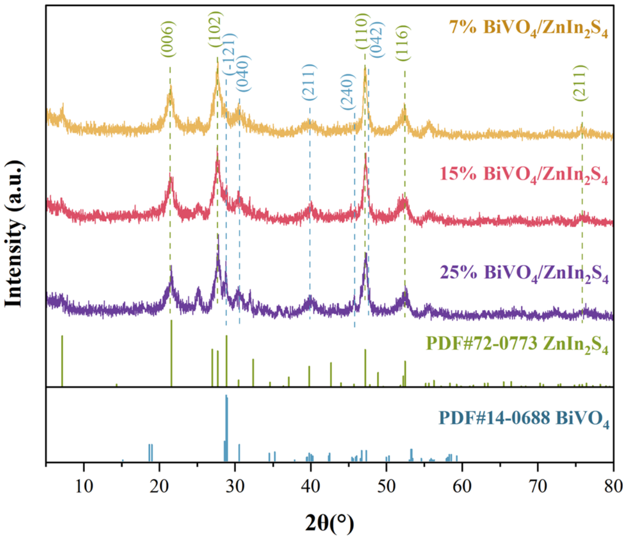

Fig. 1 XRD patterns of $BiVO_4/ZnIn_2S_4$.

As shown in Fig. S1a, the XPS spectra of $BiVO_4/ZnIn_2S_4$ confirmed that $BiVO_4/ZnIn_2S_4$ was composed of Bi, V, O, Zn, In and S elements, consistent with the XRD results. All the XPS spectra were referenced to the C 1s peak (284.0 eV) to eliminate charge effects. In Fig. S1b, prominent peaks at 164.22 eV and 158.92 eV were assigned to Bi $4f_{5/2}$ and Bi $4f_{7/2}$,[32] respectively. In Fig. S1c, the peaks at 1045.7 eV and 1022.5 eV are assigned to Zn $2p_{1/2}$ and Zn $2p_{3/2}$,[33] respectively. In Fig. S1d, the peaks at 452.9 eV and 445.3 eV could correspond to In $3d_{3/2}$ and In $3d_{5/2}$,[34] respectively. In Fig. S1e, weak peaks at 162 eV and 160 eV were attributed to the $2p_{1/2}$ and $2p_{3/2}$ of S,[35] respectively. In Fig. S1f, the peaks at 524.35 eV and 516.46 eV can be assigned as the $2p_{1/2}$ and $2p_{3/2}$ of V, respectively, indicating the sample contained the pentavalent vanadium of $BiVO_4$. Fig. S1g indicates that the O 1s XPS spectrum in $BiVO_4$ could be divided into three characteristic peaks as the O–H (531.8 eV), V–O (530.5 eV), and Bi–O (529.3 eV) bonds. From Fig. S1a–g, the binding energies corresponding to Bi 4f, V 2p, and O 1s in the $BiVO_4/ZnIn_2S_4$ composite shifted to higher energy levels compared with those of $BiVO_4$, indicating the decrease in the electron density of $BiVO_4$. Meanwhile, the binding energy of Zn 2p, In 3d, and S 2p in $BiVO_4/ZnIn_2S_4$ shifts toward lower energy compared with those of $ZnIn_2S_4$, implying an increase in the electron density of $ZnIn_2S_4$. The binding energy shift provides essential evidence for the formation of the internal electric field (IEF)[36] at the heterojunction interface: the difference in Fermi levels between $BiVO_4$ and $ZnIn_2S_4$ causes charge rearrangement at the interface. Therefore, it can be concluded that the photogenerated electrons migrated from $BiVO_4$ to the $ZnIn_2S_4$ in the $BiVO_4/ZnIn_2S_4$ composite, which provides a strong driving force for the directional migration of photogenerated carriers, meanwhile, the photocatalytic performance was enhanced by accelerating the electron and hole separation.

BET analysis is a useful method to characterize the textural properties of photocatalysts.[37] Table S1 shows that $BiVO_4/ZnIn_2S_4$ exhibits the largest specific surface area and pore size. This creates additional active sites and facilitates charge transport, thus adsorpting more pollutants and accelerating the adsorption rate, which in turn improves the photocatalytic activity. Reduced charge transport distances and optimized surface characteristics are beneficial for heterogeneous photocatalytic processes.[38]

Fig. S2 presents the FT-IR spectra of pure $BiVO_4$ and the $BiVO_4/ZnIn_2S_4$ composite. For the pure $BiVO_4$, the diffraction

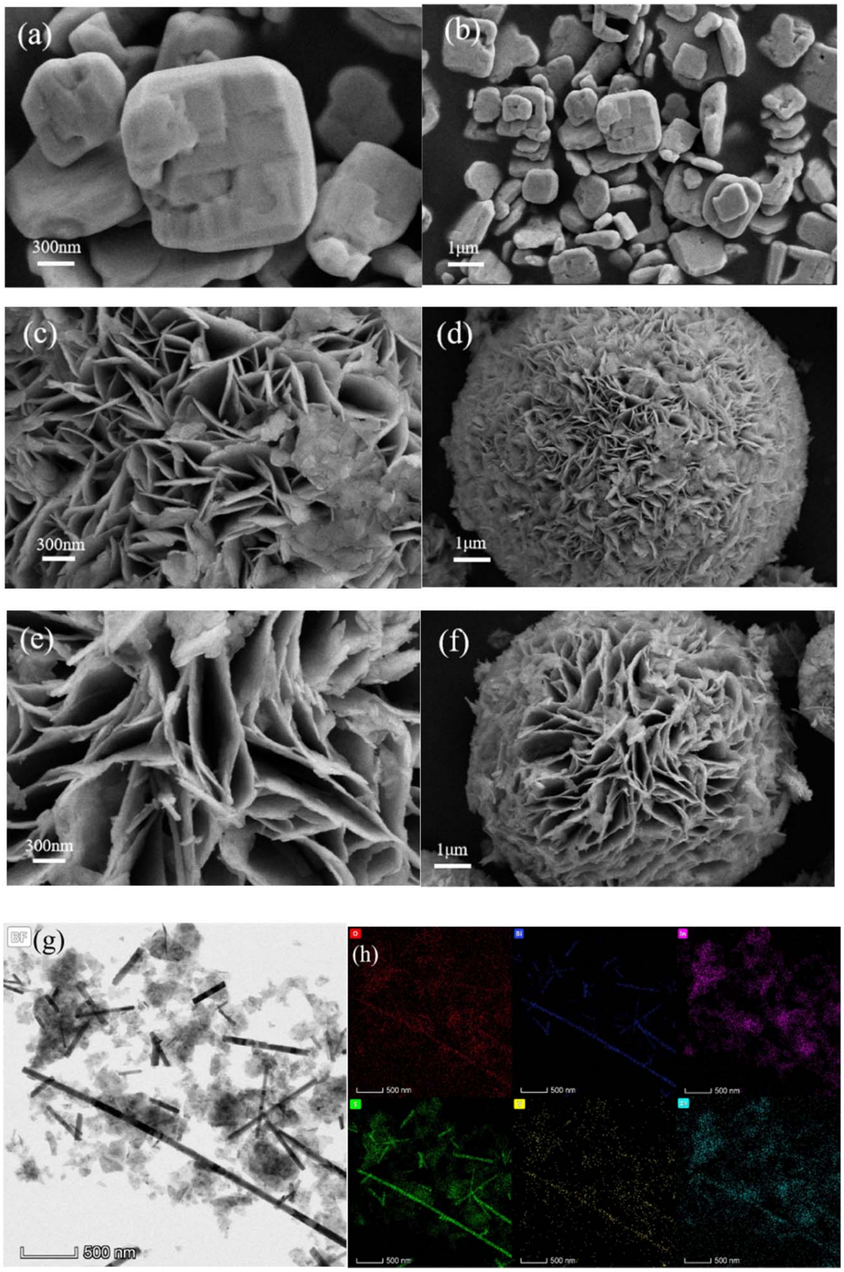

Fig. 2 SEM images of the photocatalysts: $BiVO_4$ (a and b), $ZnIn_2S_4$ (c and d), and $BiVO_4/ZnIn_2S_4$ (e and f). TEM bright-field image (g) and the corresponding EDS elemental mapping (h) of $BiVO_4/ZnIn_2S_4$.

peak at 3440.36 cm^{-1} corresponds to the O–H stretching vibrations, which is possibly related to the adsorbed water or hydroxyl group.[39] The diffraction peak of the V–O bond is located at 1382.14 cm^{-1}, and the peak at 745.84 cm^{-1} is attributed to the bending vibration of the Bi–O and O=Bi–O bonds.[40] For the $BiVO_4/ZnIn_2S_4$ composite, the 3440.36 cm^{-1}, 1403.69 cm^{-1}, and 1087.65 cm^{-1} absorption peaks represent the vibration peaks of the O–H, Zn–S,[41] and In–S bonds,[42] respectively. Based on the analysis, the FT-IR spectra of the $BiVO_4/ZnIn_2S_4$ composite exhibit the characteristic peaks of $BiVO_4$ and $ZnIn_2S_4$; moreover, compared with the spectrum of pure $BiVO_4$, the characteristic absorption peaks of the composite shifted toward higher wavenumber, suggesting that $BiVO_4$ and $ZnIn_2S_4$ are not merely physically mixed.[43]

Through UV-visible diffuse reflection analysis of the catalysts, the optical absorption characteristics and E_g of the materials involved in the composite catalyst were determined according to the relationship between UV-visible light absorption coefficient and the E_g as follows: $(\alpha h\nu)^{1/n} = K(h\nu - E_g)$,[44] where α is the absorption coefficient, h denotes Planck's constant, ν represents the incident light frequency, E_g stands for the band gap, and K is a constant. The parameter n is determined by the transition properties of the semiconductor, where $n = 1/2$ and $n = 2$ correspond to direct and indirect transitions, respectively.[45] Since $BiVO_4$ is a direct transition semiconductor,

n is 1/2.[46] As shown in Fig. S5a, it can be seen that 520 nm and 560 nm are the optical absorption edges of $BiVO_4$ and $ZnIn_2S_4$, respectively. However, the visible-light absorption range was significantly expanded after combining these two materials. The improvement stems from the broad visible-light absorption range of $ZnIn_2S_4$, which increases the absorption capacity of visible light, raises the visible-light utilization rate, and improves the photocatalytic performance. Fig. S5b shows that the E_g of $BiVO_4$, $ZnIn_2S_4$, and $BiVO_4/ZnIn_2S_4$ are 2.13 eV, 2.28 eV, and 1.93 eV, respectively. Since the photocatalytic activity largely depends on the E_g of the semiconductor photocatalyst, the $BiVO_4/ZnIn_2S_4$ composite exhibits a higher catalytic activity. The point of zero charge (PZC) of pure $BiVO_4$ is reported to be around pH 4.2,[47] while that of pure $ZnIn_2S_4$ is around pH 6.0.[48] The $BiVO_4/ZnIn_2S_4$ composite was formed by combining the two semiconductors and thus will possess the both surface charge characteristics. Therefore, it can be inferred that the PZC of the $BiVO_4/ZnIn_2S_4$ composite lies between these two values. The reaction pH in this study was 6.0; therefore, the surface of the composite is slightly negatively charged, which is not favorable for the adsorption of anionic Congo red. This indicates that the excellent photocatalytic performance of the composite is mainly attributed to efficient separation of photogenerated carriers and the generation of reactive radicals.

3.2 Photocatalytic activity

Fig. 3 summarizes the decomposition of Congo red by pure $BiVO_4$ and the $BiVO_4/ZnIn_2S_4$ composites of different ratios. After 30 minutes of dark reaction, all $BiVO_4/ZnIn_2S_4$ composites exhibited significantly higher degradation ability than that achieved with $BiVO_4$. This was due to the constitutive Z-type heterojunction between $BiVO_4$ and $ZnIn_2S_4$, which enhanced visible-light absorption and suppressed the recombination of photogenerated charge carriers, thereby improving the utilization efficiency of the photocatalyst. Thus, 7% $BiVO_4/ZnIn_2S_4$ achieved 100% degradation efficiency after 10 minutes. However, increasing the $BiVO_4$ loading led to a decline in the photocatalytic performance. The photocatalytic degradation of Congo red followed the pseudo-first-order kinetic model. The rate constant of pure $BiVO_4$ was 0.0100 min^{-1}, while those of 7% $BiVO_4/ZnIn_2S_4$, 15% $BiVO_4/ZnIn_2S_4$, and 25% $BiVO_4/ZnIn_2S_4$ composites increased to 0.1514 min^{-1}, 0.1022 min^{-1}, and 0.1050 min^{-1}, respectively, which were significantly higher than that of pure $BiVO_4$. Furthermore, the stability of the composites was tested: after six consecutive usage cycles, the Congo red degradation rate was approximate 100% (Fig. S3), proving that the prepared composite samples had high stability. Although this study did not directly validate particle stability through XRD and XPS characterization, the six-cycle tests achieved systematic validation.[49]

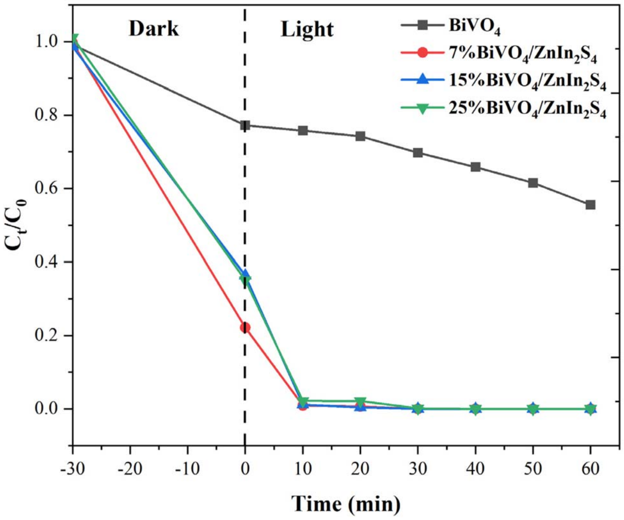

Fig. 3 Degradation rate plot of Congo red by $BiVO_4$ and $BiVO_4/ZnIn_2S_4$.

3.3 Photocatalytic mechanism

For the EPR measurements, 5,5-dimethyl-1-pyrroline-*N*-oxide (DMPO) was used as the trapping agent to detect $^{\bullet}O_2^-$ and $^{\bullet}OH$ radicals. Fig. 4a and b demonstrate that no significant free

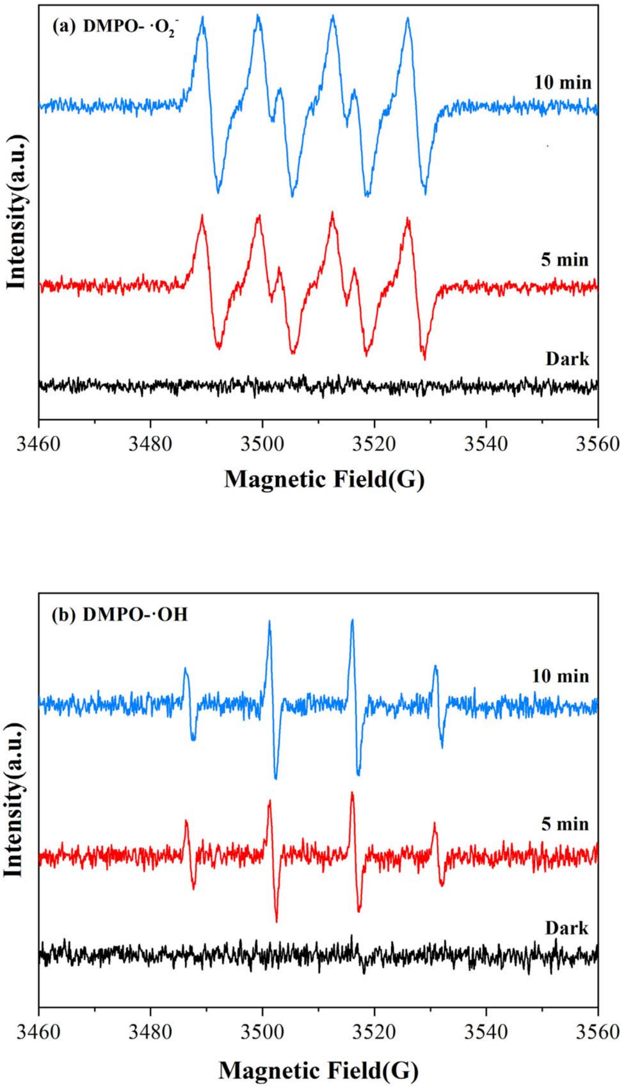

Fig. 4 EPR plots of $^{\bullet}O_2^-$ (a) and $^{\bullet}OH$ (b).

radical signal was detected under dark conditions, while light irradiation induced the emergence of characteristic EPR signals corresponding to DMPO-$^{\bullet}O_2^-$ and DMPO-$^{\bullet}$OH adducts. This confirms that both $^{\bullet}O_2^-$ and $^{\bullet}$OH radicals were generated during the photocatalytic process.

Further confirming the main active species driving Congo red degradation during the photocatalytic process, adding TEOA barely affected the degradation efficiency (Fig. S4), suggesting that h^+ was not the primary reactive species. In contrast, adding BQ and IPA suppressed the degradation rate, confirming that $^{\bullet}O_2^-$ and $^{\bullet}$OH radicals acted as the dominant reactive species under light irradiation, which is consistent with EPR results. The coexistence of ions in actual wastewater may affect degradation efficiency. According to previous studies, low concentrations of Na^+, Ca^{2+}, Mg^{2+}, Cl^-, and NO_3^- show negligible impact on degradation, as evidenced by the lack of consumption of active free radicals.[50] SO_4^{2-} may exhibit slight inhibition only at concentrations exceeding 100 mmol L^{-1}, which is significantly higher than typical wastewater levels. Furthermore, the Z-type heterojunction primarily utilizes $^{\bullet}O_2^-$ as the active species in this study, which is less susceptible to capture by CO_3^{2-}. This effectively circumvents the inhibition issues associated with conventional $^{\bullet}$OH systems;[51] therefore, $BiVO_4/ZnIn_2S_4$ shows promising application potential in complex ionic environments.

PL analysis is a powerful technique to evaluate the recombination efficiency of photogenerated electron–hole pairs, which plays a decisive role in determining the photocatalytic performance of materials.[52] As presented in Fig. 5, the three materials showed similar linear PL spectra, indicating that $ZnIn_2S_4/BiVO_4$ did not cause novel luminescence phenomena.[53] The $ZnIn_2S_4/BiVO_4$ composite exhibited a weak PL signal, indicating effective charge transfer took place at the interface of the composite. The interface effect suppressed the recombination of photogenerated charge carriers,[31] which facilitated longer charge-carrier lifetime, enhanced the photogenerated carrier separation efficiency and improved the photocatalytic performance.

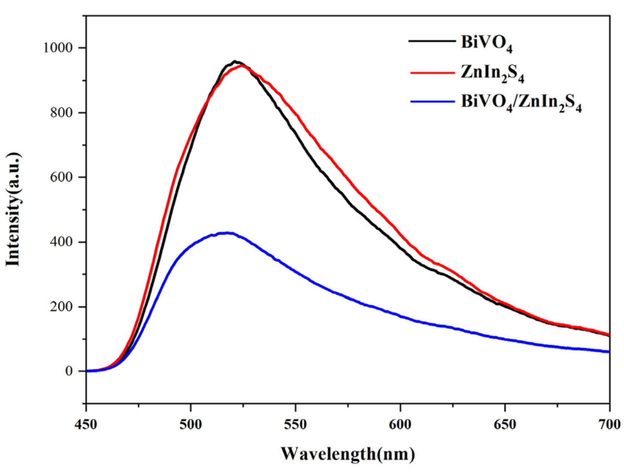

Fig. 5 PL spectra of $BiVO_4$, $ZnIn_2S_4$, and $BiVO_4/ZnIn_2S_4$.

Notably, recent studies[23,24] have proposed that the S-scheme heterojunction follows a more thermodynamically favorable electron-transfer pathway than the traditional Z-scheme. As shown in Fig. 6, the photocatalytic mechanism of $BiVO_4/ZnIn_2S_4$ is consistent with the Z-scheme based on the above test results. Specifically, if the S-scheme pathway were followed, the strongly reducing electrons in the CB of $ZnIn_2S_4$ and strongly oxidizing holes in the VB of $BiVO_4$ would recombine, leaving only weak redox carriers that cannot generate $^{\bullet}O_2^-$ and $^{\bullet}$OH radicals; however, these two radicals were detected in the radical trapping experiments. The VB of $BiVO_4$ and $ZnIn_2S_4$ were 2.77 eV (ref. 34) and 1.86 eV, respectively, and the E_g of $BiVO_4$ and $ZnIn_2S_4$ were 2.39 eV and 2.58 eV, respectively. Therefore, the CB of $BiVO_4$ and $ZnIn_2S_4$ can be calculated from the equation $E_{CB} = E_{VB} - E_g$,[54] giving E_{CB} values of 0.38 eV and −0.72 eV, respectively. The VB of $ZnIn_2S_4$ was 1.86 eV, which is less positive than the 1.99 eV (potential of $OH^-/^{\bullet}OH$); in contrast, CB of $BiVO_4$ (0.38 eV) is more positive than that of $O_2/^{\bullet}O_2^-$ (−0.33 eV).[55] After electron–hole separation, e^- would react with O_2 to generate $^{\bullet}O_2^-$, moreover, h^+ was retained in the VB of $BiVO_4$ and oxidized H_2O to generate $^{\bullet}$OH.[56]

$$\text{Photocatalyst} + h\nu \rightarrow e^- + h^+ \tag{1}$$

$$O_2 + e^- \rightarrow {}^{\bullet}O_2^- \tag{2}$$

$$OH^- + h^+ \rightarrow {}^{\bullet}OH \tag{3}$$

$$\text{Congo red} + ({}^{\bullet}OH,\ {}^{\bullet}O_2^-) \rightarrow \text{degradation product} \tag{4}$$

The toxicity of the end products of the photocatalytic degradation of Congo red depends on the degradation degree. It

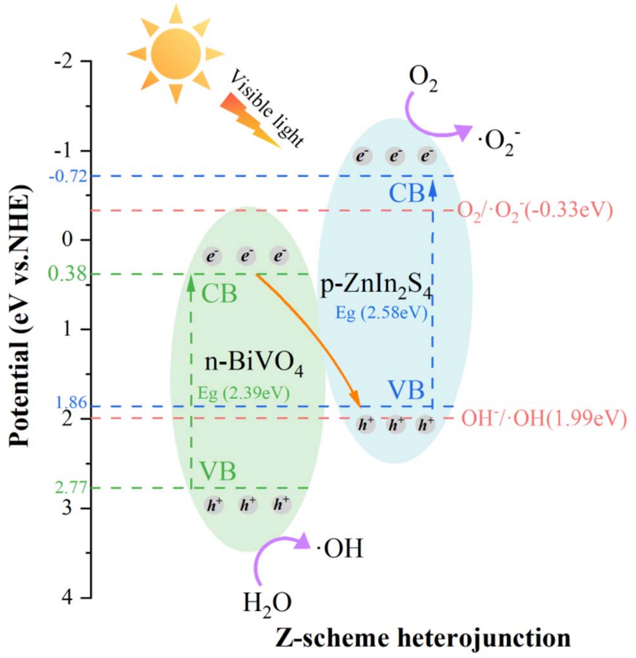

Fig. 6 Degradation mechanism of pollutants by the $BiVO_4/ZnIn_2S_4$ catalyst.

is generally accepted that the inorganic small-molecule products (CO_2, H_2O, inorganic ions, *etc.*) produced during the degradation of Congo red are basically non-toxic.[57] In this experiment, the Z-scheme $BiVO_4/ZnIn_2S_4$ photocatalyst achieved efficient deep mineralization of Congo red, so it can be reasonably inferred that the final degradation products are non-toxic.

4 Conclusion

Direct Z-scheme $BiVO_4/ZnIn_2S_4$ composite photocatalysts were successfully prepared *via* a hydrothermal method and used to degrade Congo red. Among these composites, the 7%$BiVO_4/ZnIn_2S_4$ photocatalyst exhibited the highest efficiency. The enhanced photocatalytic performance of the $BiVO_4/ZnIn_2S_4$ composites was attributed to a direct Z-scheme charge-transfer mechanism, which effectively promoted charge separation and reduced electron–hole recombination. These findings highlight the potential of $BiVO_4/ZnIn_2S_4$ composites as efficient and stable photocatalysts for environmental remediation. This work provides practical guidance for the design and fabrication of $BiVO_4$-based Z-scheme heterojunction compositions in the photocatalytic field.

Conflicts of interest

There are no conflicts to declare.

Data availability

The data supporting this article have been included as part of the supplementary information (SI). Supplementary information: Table S1 and Fig. S1–S5. See DOI: https://doi.org/10.1039/d6ra00765a.

Acknowledgements

We are grateful for the grants from the Natural Science Foundation of Heilongjiang Province of China (LH2023D003) and the Fundamental Research Funds for the Central Universities (2572022BA09).

References

1 F. Sun, F. Qiu, Y. Pan, *et al.*, Tubular Ni-NiO-TiO_2 for rapid degradation of Congo red in water under visible light, *Vacuum*, 2025, **233**, 113940, DOI: 10.1016/j.vacuum.2024.113940.

2 D. Englert, J. P. Zubrod, R. Schulz, *et al.*, Effects of municipal wastewater on aquatic ecosystem structure and function in the receiving stream, *Sci. Total Environ.*, 2013, **454–455**, 401–410, DOI: 10.1016/j.scitotenv.2013.03.025.

3 P. Borthakur, P. K. Boruah, N. Hussain, *et al.*, Specific ion effect on the surface properties of Ag/reduced graphene oxide nanocomposite and its influence on photocatalytic efficiency towards azo dye degradation, *Appl. Surf. Sci.*, 2017, **423**, 752–761, DOI: 10.1016/j.apsusc.2017.06.230.

4 C. Liang, D. Wei, S. Zhang, *et al.*, Removal of antibiotic resistance genes from swine wastewater by membrane filtration treatment, *Ecotoxicol. Environ. Saf.*, 2021, **210**, 111885, DOI: 10.1016/j.ecoenv.2020.111885.

5 S. Barua, B. S. Zakaria, T. Chung, *et al.*, Microbial electrolysis followed by chemical precipitation for effective nutrients recovery from digested sludge centrate in WWTPs, *Chem. Eng. J.*, 2019, **361**, 256–265, DOI: 10.1016/j.cej.2018.12.067.

6 B. Li, J. Liu, Q. Liu, *et al.*, Alkaline ion exchange fibers constructed by UV-induced radical polymerization for efficient uranium recovery from wastewater and seawater, *Chem. Eng. J.*, 2024, **499**, 156164, DOI: 10.1016/j.cej.2024.156164.

7 S. Bera, D. Ela-a Justina, S. Chatterjee, *et al.*, Effect of varying volumes of anaerobic microbial inoculum on biodegradation and biogas production from black water, *J. Indian Chem. Soc.*, 2024, **101**(11), 101426, DOI: 10.1016/j.jics.2024.101426.

8 K. Mabalane, N. D. Shooto and P. M. Thabede, A novel permanganate and peroxide carbon-based avocado seed waste for the adsorption of manganese and chromium ions from water, *Case Stud. Chem. Environ. Eng.*, 2024, **10**, 100782, DOI: 10.1016/j.cscee.2024.100782.

9 D. Masekela, L. K. Kganyakgo, K. D. Modibane, *et al.*, Green synthesis and enhanced photocatalytic performance of Co-Doped CuO nanoparticles for efficient degradation of synthetic dyes and water splitting, *Results Chem.*, 2025, **13**, 101971, DOI: 10.1016/j.rechem.2024.101971.

10 Z. Wang, Y. Hu, S. Wang, *et al.*, A critical review on dry anaerobic digestion of organic waste: Characteristics, operational conditions, and improvement strategies, *Renewable Sustainable Energy Rev.*, 2023, **176**, 113208, DOI: 10.1016/j.rser.2023.113208.

11 S. S. Khan, J. P. Steffy, A. T. Alfagham, *et al.*, Engineering oxygen vacancies rich nano-heterojunction for enhanced visible-light-driven photo-Fenton degradation of sulfamethoxazole, *J. Water Process Eng.*, 2025, **72**, 107542, DOI: 10.1016/j.jwpe.2025.107542.

12 M.-H. Zhang, H. Dong, L. Zhao, *et al.*, A review on Fenton process for organic wastewater treatment based on optimization perspective, *Sci. Total Environ.*, 2019, **670**, 110–121, DOI: 10.1016/j.scitotenv.2019.03.180.

13 B. Alshahrani, S. S. Fares, R. S. Alqurashi, *et al.*, Effect of gamma irradiation on the structural, optical, and electronic properties of PVC/$BiVO_4$/ZnO nanocomposite films, *Phys. Open*, 2025, **23**, 100252, DOI: 10.1016/j.physo.2025.100252.

14 S. S. Khan, J. P. Steffy, A. T. Alfagham, *et al.*, Stabilize the oxygen vacancies in $LaFeO_3$ via altering local electronic structure with CeO_2 and WS_2 QDs: A novel strategy for achieving durable visible light driven photoinactivation, *J. Water Process Eng.*, 2025, **71**, 107174, DOI: 10.1016/j.jwpe.2025.107174.

15 P. Limpachanangkul, L. Liu, P. Nimmmanterdwong, *et al.*, Statistical information review of CO_2 photocatalytic reduction via bismuth-based photocatalysts using artificial

neural network, *Alexandria Eng. J.*, 2024, **108**, 354–363, DOI: 10.1016/j.aej.2024.07.120.

16 W. Wang, T. An, G. Li, *et al.*, Earth-abundant Ni_2P/g-C_3N_4 lamellar nanohydrids for enhanced photocatalytic hydrogen evolution and bacterial inactivation under visible light irradiation, *Appl. Catal., B*, 2017, **217**, 570–580, DOI: 10.1016/j.apcatb.2017.06.027.

17 Q. Wang, J. Li, L. Xiao, *et al.*, Constructing Z-scheme Fe_3N/$BiVO_4$ heterojunction via electrostatic self-assembly toward high visible-light photocatalytic hydrogen evolution, *J. Alloys Compd.*, 2023, **935**, 168062, DOI: 10.1016/j.jallcom.2022.168062.

18 N. Akechatree, R. Rajendran, T. Rojviroon, *et al.*, Development of Z-scheme $BiVO_4$/g-C_3N_4/rGO heterojunction nanocomposite for enhanced photocatalytic degradation and antibacterial activity, *Mater. Res. Bull.*, 2025, **181**, 113119, DOI: 10.1016/j.materresbull.2024.113119.

19 Z.-H. Wei, Y.-F. Wang, Y.-Y. Li, *et al.*, Enhanced photocatalytic CO_2 reduction activity of Z-scheme CdS/$BiVO_4$ nanocomposite with thinner $BiVO_4$ nanosheets, *J. CO_2 Util.*, 2018, **28**, 15–25, DOI: 10.1016/j.jcou.2018.09.008.

20 P. Ju, L. Hao, Y. Zhang, *et al.*, Facile fabrication of a novel spindlelike MoS_2/$BiVO_4$ Z-scheme heterostructure with superior visible-light-driven photocatalytic disinfection performance, *Sep. Purif. Technol.*, 2022, **299**, 121706, DOI: 10.1016/j.seppur.2022.121706.

21 X. Ding, X. Xu, J. Wang, *et al.*, Construction of two-dimensional zinc indium sulfide/bismuth titanate nanoplate with S-scheme heterojunction for enhanced photocatalytic hydrogen evolution, *J. Colloid Interface Sci.*, 2024, **662**, 727–737, DOI: 10.1016/j.jcis.2024.02.124.

22 A. Chachvalvutikul, W. Pudkon, T. Luangwanta, *et al.*, Enhanced photocatalytic degradation of methylene blue by a direct Z-scheme Bi_2S_3/$ZnIn_2S_4$ photocatalyst, *Mater. Res. Bull.*, 2019, **111**, 53–60, DOI: 10.1016/j.materresbull.2018.10.034.

23 R. Kavitha, C. Manjunatha, J. Yu, *et al.*, Rational design and interfacial engineering of hierarchical S-scheme heterojunction and their photocatalytic applications, *EnergyChem*, 2025, **7**(4), 100159, DOI: 10.1016/j.enchem.2025.100159.

24 Q. Xu, L. Zhang, B. Cheng, *et al.*, S-Scheme Heterojunction Photocatalyst, *Chem*, 2020, **6**(7), 1543–1559, DOI: 10.1016/j.chempr.2020.06.010.

25 X. Zheng, Y. Song, Y. Liu, *et al.*, $ZnIn_2S_4$-based photocatalysts for photocatalytic hydrogen evolution via water splitting, *Coord. Chem. Rev.*, 2023, **475**, 214898, DOI: 10.1016/j.ccr.2022.214898.

26 T. W. Kim and K.-S. Choi, Nanoporous $BiVO_4$ Photoanodes with Dual-Layer Oxygen Evolution Catalysts for Solar Water Splitting, *Science*, 2014, **343**(6174), 990–994, DOI: 10.1126/science.1246913.

27 A. Chachvalvutikul, W. Pudkon, T. Luangwanta, *et al.*, Enhanced photocatalytic degradation of methylene blue by a direct Z-scheme Bi_2S_3/$ZnIn_2S_4$ photocatalyst, *Mater. Res. Bull.*, 2019, **111**, 53–60, DOI: 10.1016/j.materresbull.2018.10.034.

28 M. Imran, W. Ashraf, A. K. Hafiz, *et al.*, Synthesis and Performance Analysis of Photocatalytic Activity of $ZnIn_2S_4$ Microspheres Synthesized Using a Low-Temperature Method, *ACS Omega*, 2022, **7**(27), 22987–22996, DOI: 10.1021/acsomega.2c00945.

29 S. Majumder, N. D. Quang, C. Kim, *et al.*, Anion exchange and successive ionic layer adsorption and reaction-assisted coating of $BiVO_4$ with Bi_2S_3 to produce nanostructured photoanode for enhanced photoelectrochemical water splitting, *J. Colloid Interface Sci.*, 2021, **585**, 72–84, DOI: 10.1016/j.jcis.2020.11.081.

30 M. Li, S. Ke, X. Yang, *et al.*, S-scheme homojunction of 0D cubic/2D hexagonal $ZnIn_2S_4$ for efficient photocatalytic reduction of nitroarenes, *J. Colloid Interface Sci.*, 2024, **674**, 547–559, DOI: 10.1016/j.jcis.2024.06.177.

31 D. Feng, T. Zhang, J. Wang, *et al.*, Capacitance effect of $ZnIn_2S_4$ with delicate morphology control on photocatalytic hydrogen evolution, *Sep. Purif. Technol.*, 2025, **361**, 131283, DOI: 10.1016/j.seppur.2024.131283.

32 W. Xu, Q. Zhang, K. Xu, *et al.*, Study on visible light photocatalytic performance of $BiVO_4$ modified by graphene analogue boron nitride, *Chemosphere*, 2022, **307**(2), 135811, DOI: 10.1016/j.chemosphere.2022.135811.

33 Y. Ma, J. Xu, S. Xu, *et al.*, Construction of 3D/3D heterojunction between new noble metal free $ZnIn_2S_4$ and non-inert metal $NiMoO_4$ for enhanced hydrogen evolution performance under visible light, *Int. J. Hydrogen Energy*, 2023, **48**(69), 26707–26717, DOI: 10.1016/j.ijhydene.2023.03.286.

34 Y. Zhang, D. Chen, N. Li, *et al.*, Fabricating 1D/2D Co_3O_4/$ZnIn_2S_4$ core–shell heterostructures with boosted charge transfer for photocatalytic hydrogen production, *Appl. Surf. Sci.*, 2023, **610**, 155272, DOI: 10.1016/j.apsusc.2022.155272.

35 L. Que, L. Lu, Y. Xu, *et al.*, The $ZnIn_2S_4$/CdS hollow core-shell nanoheterostructure towards enhanced visible light photocatalytic H_2 evolution via bimetallic synergism, *Int. J. Hydrogen Energy*, 2023, **48**(12), 4708–4718, DOI: 10.1016/j.ijhydene.2022.11.019.

36 Z. S. N. Ali, A. H. Bahkali, B. Janani, *et al.*, Constructing interface chemical coupling Schottky heterojunction $NiMoO_4$/WC for enhancing photocatalytic oxidative rifampicin performance: Peroxymonosulfate activation and oxygen vacancy engineering, *J. Water Process Eng.*, 2025, **79**, 109008, DOI: 10.1016/j.jwpe.2025.109008.

37 S. S. Khan, S. Kokilavani, T. A. Alahmadi, *et al.*, Enhanced visible light driven photodegradation of rifampicin and Cr(VI) reduction activity of ultra-thin ZnO nanosheets/$CuCo_2S_4$QDs: A mechanistic insights, degradation pathway and toxicity assessment, *Environ. Pollut.*, 2024, **347**, 123760, DOI: 10.1016/j.envpol.2024.123760.

38 F. Dong, Z. Wang, Y. Sun, *et al.*, Engineering the nanoarchitecture and texture of polymeric carbon nitride semiconductor for enhanced visible light photocatalytic activity, *J. Colloid Interface Sci.*, 2013, **401**, 70–79, DOI: 10.1016/j.jcis.2013.03.034.

39 B. Alshahrani, S. S. Fares, R. S. Alqurashi, *et al.*, Effect of gamma irradiation on the structural, optical, and

electronic properties of PVC/$BiVO_4$/ZnO nanocomposite films, *Phys. Open*, 2025, **23**, 100252, DOI: 10.1016/j.physo.2025.100252.

40 S. Selvarajan, A. Suganthi, M. Rajarajan, *et al.*, Highly efficient $BiVO_4$/WO_3 nanocomposite towards superior photocatalytic performance, *Powder Technol.*, 2017, **307**, 203–212, DOI: 10.1016/j.powtec.2016.10.069.

41 Y. Zhou, W. Yang, L. Feng, *et al.*, Sunflower-disc-inspired vertical growth of 2D $ZnIn_2S_4$ on ultra-thin TiO_2: Constructing a 3D porous photocatalytic glass film for ultra-efficient organic pollutant degradation, *Appl. Catal., B*, 2025, **363**, 124782, DOI: 10.1016/j.apcatb.2024.124782.

42 J. Wang, D. Wang, X. Zhang, *et al.*, An anti-symmetric dual (ASD) Z-scheme photocatalytic system: ($ZnIn_2S_4$/Er^{3+}:$Y_3Al_5O_{12}$@$ZnTiO_3$/$CaIn_2S_4$) for organic pollutants degradation with simultaneous hydrogen evolution, *Int. J. Hydrogen Energy*, 2019, **44**(13), 6592–6607, DOI: 10.1016/j.ijhydene.2019.01.214.

43 H. Wang, W. He, X. A. Dong, *et al.*, In situ FT-IR investigation on the reaction mechanism of visible light photocatalytic NO oxidation with defective g-C_3N_4, *Sci. Bull.*, 2018, **63**(2), 117–125, DOI: 10.1016/j.scib.2017.12.013.

44 J. Tauc, Absorption edge and internal electric fields in amorphous semiconductors, *Mater. Res. Bull.*, 1970, **5**(8), 721–729, DOI: 10.1016/0025-5408(70)90112-1.

45 K. Wang, X. Wu, G. Zhang, *et al.*, $Ba_5Ta_4O_{15}$ nanosheet/$AgVO_3$ nanoribbon heterojunctions with enhanced photocatalytic oxidation performance: hole dominated charge transfer path and plasmonic effect insight, *ACS Sustainable Chem. Eng.*, 2018, **6**(5), 6682–6692, DOI: 10.1021/acssuschemeng.8b00477.

46 W. Li, R. Yu, M. Li, *et al.*, Photocatalytical degradation of diclofenac by Ag-BiOI-rGO: Kinetics, mechanisms and pathways, *Chemosphere*, 2019, **218**, 966–973, DOI: 10.1016/j.chemosphere.2018.11.185.

47 M. Imran, W. Ashraf, A. K. Hafiz, *et al.*, Synthesis and Performance Analysis of Photocatalytic Activity of $ZnIn_2S_4$ Microspheres Synthesized Using a Low-Temperature Method, *ACS Omega*, 2022, **7**(27), 22987–22996, DOI: 10.1021/acsomega.2c00945.

48 M. Anjum, R. Kumar and M. A. Barakat, Visible light driven photocatalytic degradation of organic pollutants in wastewater and real sludge using ZnO–ZnS/Ag_2O–Ag_2S nanocomposite, *J. Taiwan Inst. Chem. Eng.*, 2017, **77**, 227–235, DOI: 10.1016/j.jtice.2017.05.007.

49 J. P. Steffy, A. T. Alfagham, A. M. Elgorban, *et al.*, Morphology transition engineering of WO_3 from 1D nanorods to single-crystalline 3D nanocubes grafted with 2D g-C_3N_4 decorated with 0D SnS_2 QDs for pharmaceutical waste photodegradation, *J. Water Process Eng.*, 2025, **69**, 106728, DOI: 10.1016/j.jwpe.2024.106728.

50 X. Xiang, M. Zhang, Q. Huang, *et al.*, Construction of S-scheme $CuInS_2$/$ZnIn_2S_4$ heterostructures for enhanced photocatalytic activity towards Cr(VI) removal and antibiotics degradation, *Chemosphere*, 2024, **352**, 141351, DOI: 10.1016/j.chemosphere.2024.141351.

51 G. Zhou, C. C. Aletsee, A. Lemperle, *et al.*, Water Oxidation and Degradation Mechanisms of $BiVO_4$ Photoanodes in Bicarbonate Electrolytes, *ACS Catal.*, 2025, **15**(15), 13048–13058, DOI: 10.1021/acscatal.5c03025.

52 S. Swetha, T. Awad Alahmadi, M. Javed Ansari, *et al.*, Strategically tailored double S-scheme heterojunction in h-MoO_3 doped $Bi_7O_9I_3$ decorated with Cr–CdS quantum dots for efficient photocatalytic degradation of phenolics, *J. Cleaner Prod.*, 2024, **449**, 141656, DOI: 10.1016/j.jclepro.2024.141656.

53 C. Wu, Y. Fang, A. H. Tirusew, *et al.*, Photochemical oxidation mechanism of microcystin-RR by p-n heterojunction Ag/Ag_2O-$BiVO_4$, *Chin. J. Catal.*, 2017, **38**(2), 192–198, DOI: 10.1016/s1872-2067(16)62583-4.

54 H.-Q. Jiang, H. Endo, H. Natori, *et al.*, Fabrication and efficient photocatalytic degradation of methylene blue over CuO/$BiVO_4$ composite under visible-light irradiation, *Mater. Res. Bull.*, 2009, **44**(3), 700–706, DOI: 10.1016/j.materresbull.2008.06.007.

55 F. Yang, X. Yu, Z. Liu, *et al.*, Preparation of Z-scheme $CuBi_2O_4$/Bi_2O_3 nanocomposites using electrospinning and their enhanced photocatalytic performance, *Mater. Today Commun.*, 2021, **26**, 101735, DOI: 10.1016/j.mtcomm.2020.101735.

56 X. Wang, X. Wang, H. Zhang, *et al.*, Photothermal-assisted photocatalytic degradation of tetracycline in simulated natural water by $BiVO_4$/$CuBi_2O_4$ Z-scheme heterojunction: Mechanisms insight, degradation pathways and toxicity assessment, *Process Saf. Environ. Prot.*, 2024, **188**, 1292–1305, DOI: 10.1016/j.psep.2024.06.042.

57 S. Muthalagu, A. MohamedAsik, M. Selvaraj, *et al.*, Green synthesis of copper oxide nanoparticles using Ficus pumila and their multifunctional biomedical and environmental applications, *Bioorg. Chem.*, 2025, **167**, 109272, DOI: 10.1016/j.bioorg.2025.109272.